Simulating Boundary Fields of Arbitrary-shaped Objects in a Reverberation Chamber

Qian Xu [1], Kai Chen [1,3], Chun Ren [2], Xueqi Shen [3], and Yi Huang [4]

[1] College of Electronic and Information Engineering
Nanjing University of Aeronautics and Astronautics, Nanjing 211106, China
emxu@foxmail.com, chenkay@nuaa.edu.cn

[2] Dassault Systèmes (Shanghai) Information Technology, co. Ltd. Beijing Branch, Beijing, 100025, China
chun.ren@3ds.com

[3] Nanjing Rongce Testing Technology Ltd, Nanjing 211112, China
george@emcdir.com

[4] Department of Electrical Engineering and Electronics
The University of Liverpool, Liverpool, L69 3GJ, United Kingdom
yi.huang@liverpool.ac.uk

Abstract ─ In a reverberation chamber, analytical solutions exist in very limited scenarios for the distribution of the boundary fields. For arbitrary-shaped objects, analytical solutions may not exist. To solve this problem, a general numerical method is proposed to obtain the mean field distribution near arbitrary-shaped objects in a random diffused-wave environment. The proposed method combines the full-wave method and the Monte-Carlo method; the numerical results are validated and compared with that from analytical equations. The proposed method can be applied to arbitrary-shaped objects with general material properties.

Index Terms ─ Boundary fields, Monte-Carlo simulation, plane wave model, reverberation chamber.

I. INTRODUCTION

Reverberation chambers (RCs) have been widely used in electromagnetic compatibility (EMC) [1] and over-the-air (OTA) testing [2-5] in recent years. New applications include antenna measurement [6], radar cross section measurement [7], and channel emulation [3]. Ideally, a statistically homogeneous and isotropic random multipath environment can be created in an RC. When the field point is far from the boundaries and stirrers (typically larger than $\lambda/4$ [1]), the field can be considered statistically uniform and isotropic. However, because of the boundary conditions (e.g., the tangential component of E-field is nearly zero $E_t = 0$ on the metallic boundaries), the field statistics close to the boundaries deviate from ideal values and is no longer uniform and isotropic [1, 3]. Generally, how the power density ($\langle|E_x|^2\rangle$, $\langle|E_y|^2\rangle$ or $\langle|E_z|^2\rangle$) distributes around an arbitrary-shaped object remains unsolved. This paper is aimed to solve this problem by applying the plane wave model (PWM) directly [3, 8].

Luckily, typical boundary fields such as planar, right-angle bend and right-angle corners have analytical solutions [9, 10]. In these cases, the distribution of the mean value of the boundary fields can be expressed analytically as a function of (x, y, z) coordinates. At high frequency limit, a very efficient model is proposed in [11, 12] by using the diffusion equation to obtain a system-level description. In this paper, we apply the PWM using the full-wave simulation and combine the results using the Monte-Carlo method [13-16]; the method is a direct method from the first principle and can be applied to arbitrary-shaped boundary shapes and material properties.

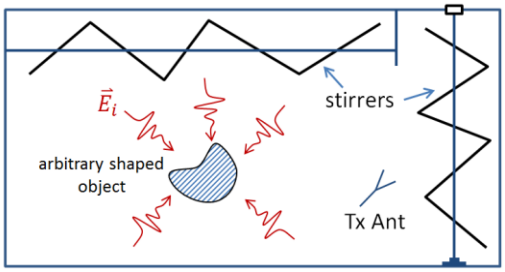

Fig. 1. An arbitrary shaped object in a random field environment (reverberation chamber).

The algorithm is detailed in Section II and the

Submitted On: July 29, 2021
Accepted On: August 22, 2021
https://doi.org/10.47037/2021.ACES.J.360902

simulated results are validated in Section III, general scenarios are investigated in Section IV and conclusions are summarized in Section V.

II. ALGORITHM

For an arbitrary-shaped object in an RC in Fig. 1, when the RC is well stirred, the random wave environment can be modeled using multiple plane waves. Each incident plane wave can be expressed as:

$$\vec{E}_i = \vec{A}_i e^{-j\vec{k}_i\cdot\vec{r}_i}, \quad (1)$$

where i represents ith incident wave, k is the wave number, $\vec{r} = (x, y, z)^T$ represents the field point and $\vec{A}_i$ is a complex vector which represents the amplitude and initial phase of the plane wave. For many random incident waves we have [13]:

$$\vec{E}_{inc} = \sum_{i=1}^{N} \vec{E}_i = \sum_{i=1}^{N} \vec{A}_i e^{-j\vec{k}_i\cdot\vec{r}_i}, \quad (2)$$

where the amplitude and phase of $\vec{A}_i$ are Rayleigh and uniform distributed, respectively. When the plane wave number N approaches to infinity, (2) is the well-known PWM which is also written as [3]:

$$\vec{E}_{inc} = \iint_{4\pi} \vec{A}(\Omega)\, e^{-j\vec{k}\cdot\vec{r}}\, \mathrm{d}\Omega\,, \quad (3)$$

where $\iint_{4\pi}[\cdot]\,\mathrm{d}\Omega$ means the integral over a unit sphere. As we can only simulate finite N numerically, we start from (2) to detail the algorithm.

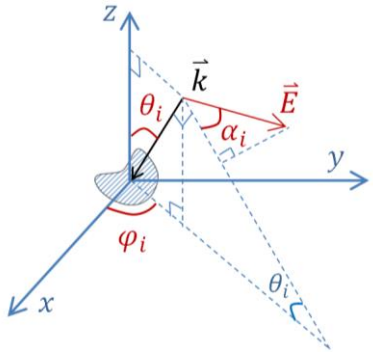

Fig. 2. Angle definitions of an incident plane wave.

For each plane wave, the wave propagation direction can be expressed as:

$$k_{xi} = -\sin(\theta_i)\cos(\varphi_i)$$
$$k_{yi} = -\sin(\theta_i)\sin(\varphi_i)$$
$$k_{zi} = -\cos(\theta_i), \quad (4)$$

and the E-field direction can be expressed as:

$$E_{xi} = \cos(\varphi_i)\cos(\theta_i)\cos(\alpha_i) - \sin(\varphi_i)\sin(\alpha_i)$$
$$E_{yi} = \sin(\varphi_i)\cos(\theta_i)\cos(\alpha_i) + \cos(\varphi_i)\sin(\alpha_i)$$
$$E_{zi} = -\sin(\theta_i)\cos(\alpha_i), \quad (5)$$

where θ_i and φ_i are the polar angle and azimuth angle respectively, α_i is the polarization angle. The definitions are illustrated in Fig. 2. Only two α values (0º and 90º) are necessary which represents TE and TM waves respectively.

For each incident wave $\vec{E}_i$, the scattering problem can be solved by using the Finite Integral Time Domain (FITD) method in CST, the E-field in the solving volume can be solved as $\vec{E}_{iTot}$ (normalized to 1 V/m incident wave). Simulations using FDTD and TLM method for RC performance analysis have been detailed in [17-21]. When the system is linear, the total field in the solving volume can be obtained as $\vec{E}_{Tot} = \sum_{i=1}^{N} A_i \exp(j\delta_i)\vec{E}_{iTot}$ for N plane waves incident simultaneously with random amplitude A_i and δ_i phase. By repeating this process M times with Monte-Carlo simulations, the mean value of the square of the total fields (power density) can be obtained. The probability density function (PDF) of the power density is still exponential distribution but with different mean parameters, thus we focus on the mean values in the simulation.

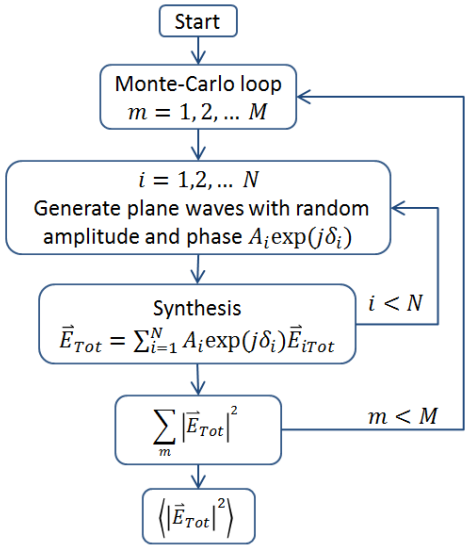

Fig. 3. The workflow of the full-wave Monte-Carlo simulation.

Table 1: Simulation scenarios

	Scenarios	Simulation Time FW+MC (hours)
Analytical scenarios	Vacuum cube	13.2+3.9
	Right-angle bend	6.1+3.9
	Right-corner	6.4+3.9
General scenarios	Arbitrary-angle bend	6.4+3.9
	Dielectric cube	17.8+3.9
	Receiving antenna	6.4+3.9
	Half-space aperture	4.6+3.9

The workflow of the full-wave Monte-Carlo simulation (FWMC) is illustrated in Fig. 3. Note that the FITD simulation only needs to be performed for N times, each $\vec{E}_{iTot}$ is saved in memory and no full-wave simulation is necessary in the Monte-Carlo simulation.

In the next section (Section III), we validate the proposed method using models with have analytical solutions. In Section IV, we apply the FWMC method to general scenarios. The simulation scenarios are given in Table 1, in which FW and MC represent full-wave simulation and Monte-Carlo simulation respectively. Since we use the same sampling number for $\vec{E}_{iTot}$ in all models, the MC simulation time are the same.

III. VALIDATIONS

In the FWMC simulation, we use 642 sets of (θ_i, φ_i) (illustrated in Fig. 4) for $\vec{k}$ vectors and each incident wave has two polarizations with $\alpha = 0°$ and $\alpha = 90°$, thus $N = 1284$ incident waves are simulated (the magnitude of the incident wave is normalized to 1 V/m). After each simulation, the total fields in the solving volume are saved as $E_{xiTot}(x, y, z)$, $E_{yiTot}(x, y, z)$ and $E_{ziTot}(x, y, z)$. After the full-wave simulation, the Monte-Carlo simulation in Fig. 3 is performed with $M = 10000$. The M value can be understood as the number of independent stirrer positions in an ideal RC, as for each value of M, a new set of A_i and δ_i are generated.

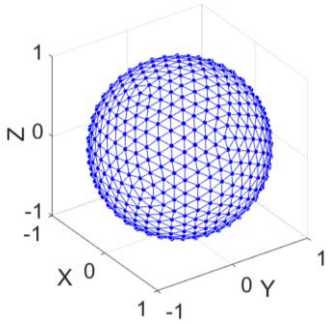

Fig. 4. 642 incident wave directions on a unit sphere are used in the full-wave simulation.

To normalize $\langle|E_{xTot}|^2\rangle$ to 1 at fields far from boundaries, the magnitude of the incident plane wave A_i has a Rayleigh distribution and the PDF is [3]:

$$p_A(x) = \frac{x}{\sigma^2} e^{-\frac{x^2}{2\sigma^2}}, \quad x = A_i, \tag{6}$$

with $\sigma = \sqrt{3/2}/\sqrt{N}$. The initial phase δ_i has a uniform distribution in $(0, 2\pi]$. To verify the proposed method we simulate a vacuum cube, a right-angle bend and a right-angle corner as they have analytical solutions.

A. A vacuum cube

We first use a vacuum cube in Fig. 5 (a) to validate the method, the electrical dimensions are $4\lambda \times 4\lambda \times 4\lambda$. Since there is no scatter in the solving volume, the error can be explained as the numerical noise level. The simulated $\langle|E_{xTot}|^2\rangle$ is illustrated in Fig. 5 (b), as can be seen, the values are very close to 1 and the relative standard deviation (which is also the field uniformity (FU)) is about 1% (0.05 dB). This agrees well with the theoretical value from the central limit theorem which is $1/\sqrt{M}$. This also means that the statistical noise level is about -20 dB for $M = 10000$. The FU in the simulation volume is given in Fig. 6 for different M and N values. The unit sphere is decomposed uniformly with $4^{p-1} \times 10 + 2$ ($p = 1, 2, \ldots$) points, and the plane wave number is $4^{p-1} \times 20 + 4$. The theoretical curve of $10\log_{10}(1 + 1/\sqrt{M})$ is also given. As can be seen, very good agreement is obtained; the FU is dominated by M and is not sensitive to N in free space.

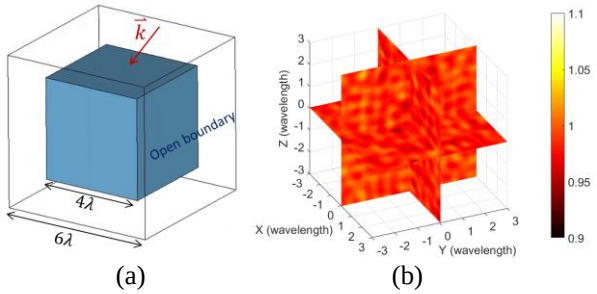

(a) (b)

Fig. 5. (a) A vacuum cube, and (b) simulated $\langle|E_{xTot}|^2\rangle$, the plots for $\langle|E_{yTot}|^2\rangle$ and $\langle|E_{zTot}|^2\rangle$ are similar.

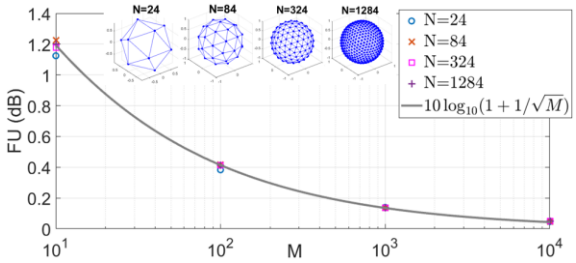

Fig. 6. Simulated FU with different M and N values.

B. A right-angle bend

A right-angle bend with two finite plates are presented in Fig. 7 (a), the edge length is 4λ. Note that when the plates are infinitely large, analytical solutions exist [3]:

$$\langle|E_{zTot}(x, y, z)|^2\rangle = \frac{E_0^2}{3}\left[1 - \rho_t(2y) - \rho_t(2x) + \rho_t\left(2\sqrt{x^2 + y^2}\right)\right], \tag{7}$$

$$\langle|E_{xTot}(x, y, z)|^2\rangle = \frac{E_0^2}{3}[1 - \rho_t(2y) + \rho_l(2x) - \frac{y^2}{x^2 + y^2}\rho_t(2\sqrt{x^2 + y^2}) - \frac{x^2}{x^2 + y^2}\rho_l(2\sqrt{x^2 + y^2})], \tag{8}$$

where $\rho_t(\cdot)$ and $\rho_l(\cdot)$ are defined as:

$$\rho_t(r) = \frac{3}{2}\left[\frac{\sin(kr)}{kr} - \frac{1}{(kr)^2}\left(\frac{\sin(kr)}{kr} - \cos(kr)\right)\right], \quad (9)$$

$$\rho_l(r) = \frac{3}{(kr)^2}\left[\frac{\sin(kr)}{kr} - \cos(kr)\right]. \quad (10)$$

The simulated results are illustrated in Figs. 7 (b)-(d). Comparisons between numerical and analytical results along the radial direction ($x = y$, $z = 0$) are given in Fig. 7 (d). As expected, the simulated results agree well with the analytical results, and the negative r represents the other side of right-angle bend. The plot for $\langle|E_{yTot}|^2\rangle$ is not shown as it is similar to $\langle|E_{xTot}|^2\rangle$.

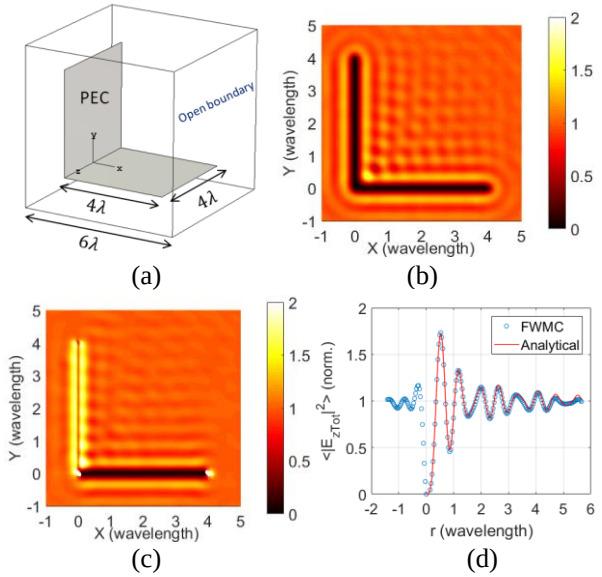

Fig. 7. (a) A right-angle bend, (b) simulated $\langle|E_{zTot}|^2\rangle$, (c) simulated $\langle|E_{xTot}|^2\rangle$, and (d) a comparison between results from FWMC and analytical equation.

C. A right-angle corner

A right-corner with 4-wavelength length is shown in Fig. 8 (a). When the plates are infinitely large, the analytical solution for $\langle|E_{zTot}|^2\rangle$ is [3]:

$$\langle|E_{zTot}(x,y,z)|^2\rangle = \frac{E_0^2}{3}[1 - \rho_t(2x) - \rho_t(2y) + \rho_t\left(2\sqrt{x^2+y^2}\right) + \rho_l(2z) - \frac{x^2}{x^2+z^2}\rho_t\left(2\sqrt{x^2+z^2}\right) - \frac{z^2}{x^2+z^2}\rho_l\left(2\sqrt{x^2+z^2}\right) - \frac{y^2}{y^2+z^2}\rho_t\left(2\sqrt{y^2+z^2}\right) - \frac{z^2}{y^2+z^2}\rho_l\left(2\sqrt{y^2+z^2}\right) + \frac{x^2+y^2}{x^2+y^2+z^2}\rho_t\left(2\sqrt{x^2+y^2+z^2}\right) + \frac{z^2}{x^2+y^2+z^2}\rho_l\left(2\sqrt{x^2+y^2+z^2}\right)]. \quad (11)$$

We apply the FWMC simulation and the results are illustrated in Fig. 8 (b). Comparisons between numerical and analytical results along the radial direction ($x = y = z = r/\sqrt{3}$) are given in Fig. 8 (c). Not surprisingly, good agreement is obtained. The plot for $\langle|E_{xTot}|^2\rangle$ and $\langle|E_{yTot}|^2\rangle$ are not shown as they are similar. It is interesting to note that for negative r close to 0, the field strength varies drastically because of the sharp corner.

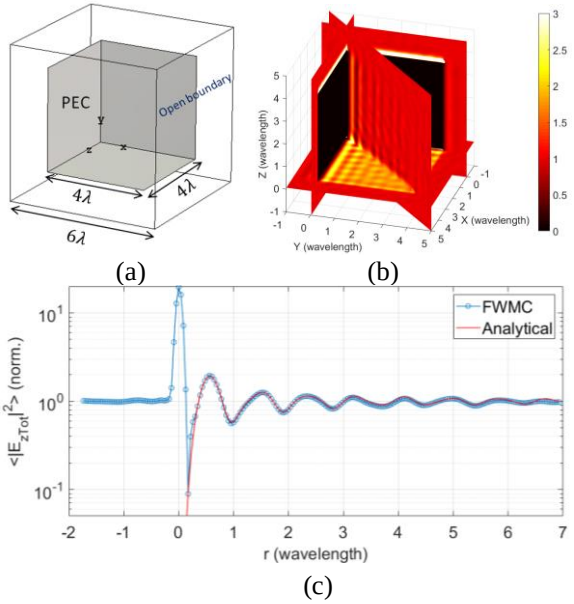

Fig. 8. (a) A right-angle corner, (b) simulated $\langle|E_{zTot}|^2\rangle$, and (c) a comparison between results from FWMC and analytical equation, note that because of the finite mesh resolution, small error exist when r is close to zero.

We have verified the numerical results in three specific scenarios and the results are correct. In the next section, we apply this method to more general scenarios.

IV. GENERAL SCENARIOS

In this section we apply the FWMC method to general scenarios, in which four types of models are demonstrated: arbitrary angle bends, dielectric objects, a receiving antenna and a half-space aperture.

A. Arbitrary angle bends

For a right-angle bend, analytical solution exists. For a bend with an arbitrary angle γ, the results can be obtained by using the FWMC method which are illustrated in Figs. 9 (a)-(g). The simulation model is given in Fig. 9 (a) and the plots for $\langle|E_{xTot}|^2\rangle$, $\langle|E_{yTot}|^2\rangle$ and $\langle|E_{zTot}|^2\rangle$ in the cut plane $z = 0$ are illustrated in Figs. 9 (b)-(d) and Figs. 9 (e)-(g) with $\gamma = 30°$ and $\gamma = 60°$ respectively. Not surprisingly, when γ becomes smaller, the FU in the corner becomes poorer.

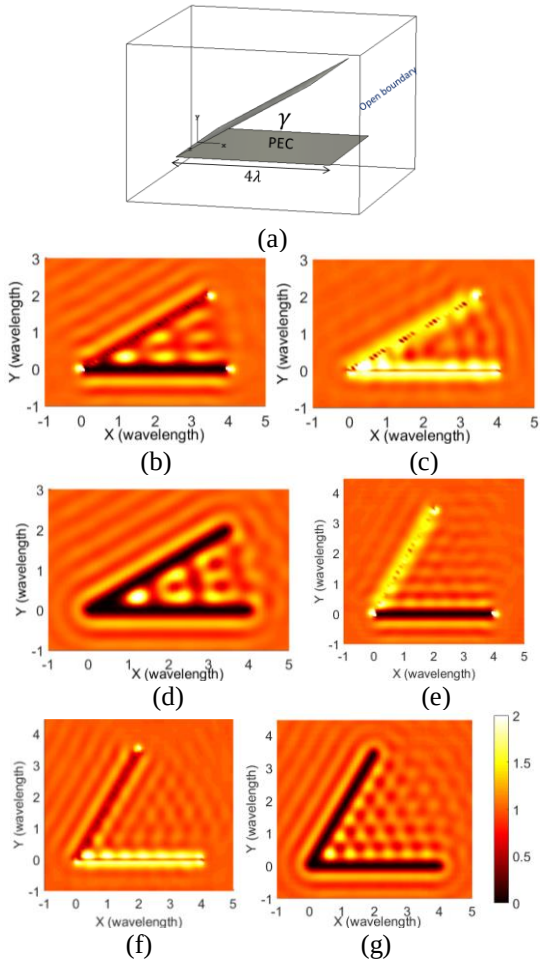

Fig. 9. (a) A bend with angle α, (b) simulated $\langle|E_{xTot}|^2\rangle$, $\gamma = 30°$, (c) simulated $\langle|E_{yTot}|^2\rangle$, $\gamma = 30°$, (d) simulated $\langle|E_{zTot}|^2\rangle$, $\gamma = 30°$, (e) simulated $\langle|E_{xTot}|^2\rangle$, $\gamma = 60°$, (f) simulated $\langle|E_{yTot}|^2\rangle$, $\gamma = 60°$, and (g) simulated $\langle|E_{zTot}|^2\rangle$, $\gamma = 60°$.

B. Dielectric objects

A dielectric block is shown in Fig. 10 with relative permittivity ε_r, the dielectric block is placed in an ideal multipath environment. The simulated $\langle|E_{zTot}|^2\rangle$ are illustrated in Figs. 10 (b)-(d) for $\varepsilon_r = 2$, 5 and 10 respectively. Because of the symmetry, only $\langle|E_{zTot}|^2\rangle$ are plots in Figs. 10 (b)-(d). The fields on the line $y = 0$, $z = 0$ are extracted and given in Fig. 10 (e). It is interesting to note that the field inside the dielectric is not statistically uniform although the environment is statistically uniform. When ε_r increases, both the inside E-field and the nonunifomity increases. This model can be used to simulate the heating power distribution of an arbitrarily shaped object inside a microwave oven.

An interesting example is the sparking of grapes in a household microwave oven [22]. A similar model in [22] is shown in Fig. 11 (a) with two dielectric spheres gapped with 1mm. The power density of $\langle|E_{xTot}|^2\rangle$ is illustrated in Figs. 11 (b) and (c). The interesting effect as in [22] is observed, the power density is enhanced greatly (more than 100 times) between the two spheres.

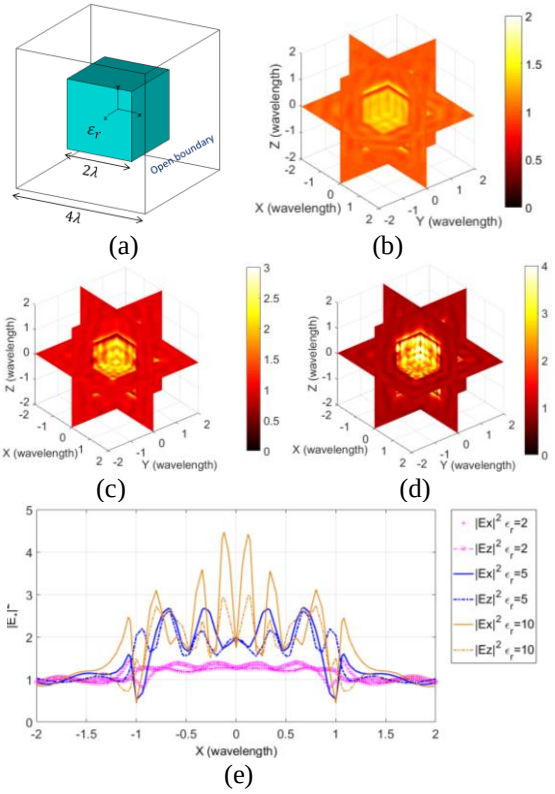

Fig. 10. (a) A dielectric block with relative permittivity ε_r, simulated $\langle|E_{zTot}|^2\rangle$ for (b) $\varepsilon_r = 2$, (c) $\varepsilon_r = 5$, (d) $\varepsilon_r = 10$, and (e) extracted plots on the line $y = 0$, $z = 0$, $\langle|E_{yTot}|^2\rangle$ are not shown as they are the same as $\langle|E_{zTot}|^2\rangle$.

C. A receiving antenna

A horn antenna working in receiving mode is shown in Fig. 12 (a). The simulated mean power densities are illustrated in Figs. 12 (b)-(d). Since the horn antenna is y-polarized, $\langle|E_{yTot}|^2\rangle$ gives smaller values than $\langle|E_{xTot}|^2\rangle$ and $\langle|E_{zTot}|^2\rangle$ in the horn.

D. A half-space aperture

When two RCs are contiguous or nested in to measure the shielding effectiveness of a planar material, we have a half-space aperture model. A half-space aperture with dimensions of $2\lambda \times 2\lambda$ is shown in Fig. 13 (a). The random incident waves are from $+z$ half space. In the FMWC simulation, we only need to generate half number of plane waves in Fig. 4. The simulated mean power densities are illustrated in Figs. 13 (b)-(c) in which we can identify how random waves diffused through an aperture and apply this method to arbitrary shaped apertures [23].

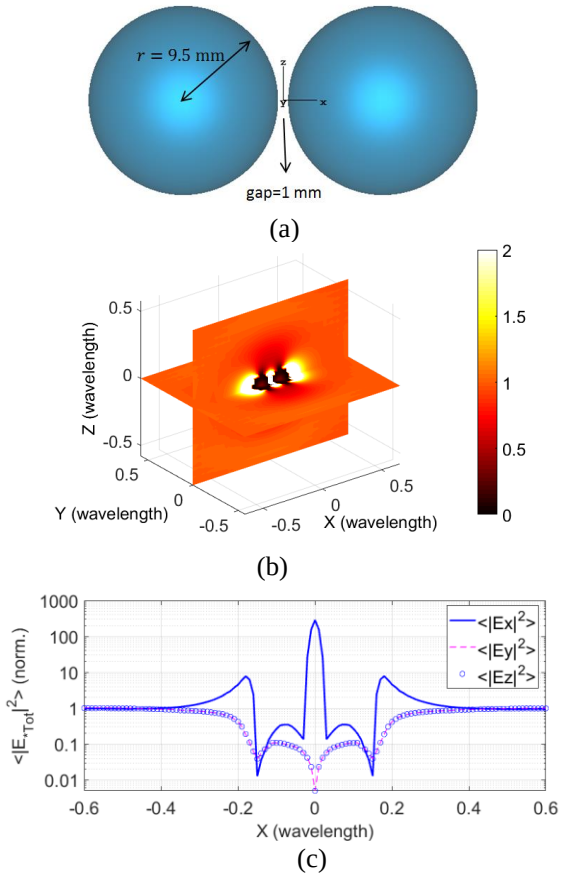

Fig. 11. (a) Two spheres gapped with 1 mm, the material is set as sea water, (b) simulated $\langle|E_{xTot}|^2\rangle$, and (c) extracted plots on the line $y = 0, z = 0$.

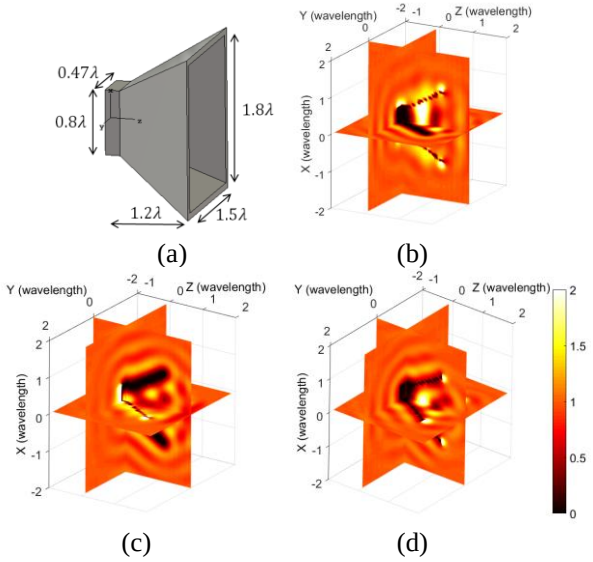

Fig. 12. (a) A horn antenna, (b) simulated $\langle|E_{xTot}|^2\rangle$, (c) $\langle|E_{yTot}|^2\rangle$, and (d) $\langle|E_{zTot}|^2\rangle$.

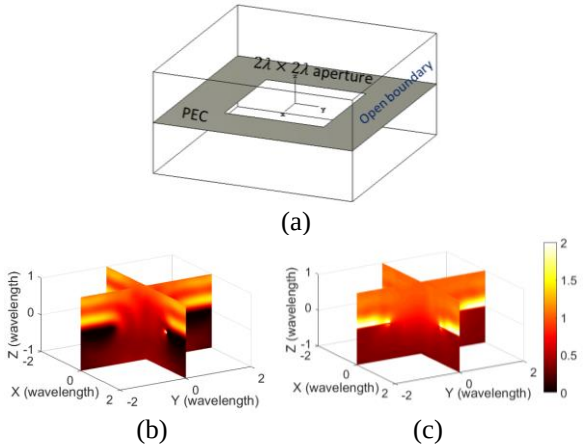

Fig. 13. (a) A half-space aperture, (b) simulated $\langle|E_{xTot}|^2\rangle$, and (c) simulated $\langle|E_{zTot}|^2\rangle$.

V. CONCLUSIONS

We have proposed the FWMC method in this paper and validated the results with analytical equations. The method is from the first principle of PWM and has been applied to general scenarios with arbitrary angle bends, dielectric materials, a receiving antenna and a half-space problem.

For the models in this paper, the simulation time for each plane wave incident is less than 2 minutes and the total simulation times for 1284 incident waves are less than 43 hours (on a computer workstation). The Monte-Carlo simulation consumes less than 4 hours for $M = 10000$. Since each plane wave is independent with others, the parameter sweep process (for each plane wave) can be parallelized with more computers.

Compared with the diffusion equation model, although the accuracy of this method is very high, the memory consumption for electrically large objects is significant. However, for waves far from scatterers, the mean power density becomes uniform in a well-stirred condition and the simulation could be unnecessary. A typical distance of at least $\lambda/4$ from any scatterers is suggested for EMC applications [1]. For non-ideal reverberant environment, this method could be combined with the diffusion equation model to provide more accurate boundary conditions.

ACKNOWLEDGMENT

This work was supported in part by the National Natural Science Foundation of China under Grants 61701224 and in part by Nanjing Rongce Testing Technology Ltd.

REFERENCES

[1] IEC 61000-4-21, *Electromagnetic compatibility (EMC) – Part 4-21: Testing and measurement*

techniques – Reverberation chamber test methods, IEC Standard, Ed 2.0, 2011-01.

[2] CTIA, *Test Plan for Wireless Large-Form-Factor Device Over-the-Air Performance*, ver. 1.2.1, Feb. 2019.

[3] D. A. Hill, *Electromagnetic Fields in Cavities: Deterministic and Statistical Theories*. Wiley-IEEE Press, USA, 2009.

[4] X. Chen, J. Tang, T. Li, S. Zhu, Y. Ren, Z. Zhang, and A. Zhang, "Reverberation chambers for over-the-air tests: An overview of two decades of research," *IEEE Access*, vol. 6, pp. 49129-49143, 2018.

[5] Q. Xu and Y. Huang, *Anechoic and Reverberation Chambers: Theory Design and Measurements*. Wiley-IEEE Press, USA, 2019.

[6] M. S. Castañer, "Review of recent advances and future challenges in antenna measurement," *Applied Computational Electromagnetics Society Journal*, vol. 33, no. 2, pp. 99-102, Jan. 2018.

[7] A. Sorrentino, G. Ferrara, M. Migliaccio, and S. Cappa, "Measurements of backscattering from a dihedral corner in a reverberation chamber," *Applied Computational Electromagnetics Society Journal*, vol. 33, no. 1, pp. 91-93, Jan. 2018.

[8] D. A. Hill, "Plane wave integral representation for fields in reverberation chambers," *IEEE Trans. Electromagn. Compat.*, vol. 40, no. 3, pp. 209-217, Aug. 1998.

[9] D. A. Hill, "Boundary fields in reverberation chambers," *IEEE Trans. Electromagn. Compat.*, vol. 47, no. 2, pp. 281-290, May 2005.

[10] A. Somani, S. Gorla, M. Magdowski, and R. Vick, "Measurement of boundary fields in a reverberation chamber," *10th International Symposium on Electromagnetic Compatibility*, pp. 123-127, 2011.

[11] I. D. Flintoft and J. F. Dawson, "3D electromagnetic diffusion models for reverberant environments," *International Conference on Electromagnetics in Advanced Applications (ICEAA)*, pp. 511-514, 2017.

[12] I. D. Flintoft, A. C. Marvin, F. I. Funn, L. Dawson, X. Zhang, M. P. Robinson, and J. F. Dawson, "Evaluation of the diffusion equation for modeling reverberant electromagnetic fields," *IEEE Trans. Electromagn. Compat.*, vol. 59, no. 3, pp. 760-769, June 2017.

[13] J. M. Ladbury, "Monte Carlo simulation of reverberation chambers," *Gateway to the New Millennium. 18th Digital Avionics Systems Conference. Proceedings (Cat. No.99CH37033)*, pp. 10.C.1-10.C.1, 1999.

[14] Y. Li, X. Zhao, L. Yan, K. Huang, and H. Zhou, "Probabilistic-statistical model based on mode expansion of the EM field of a reverberation chamber and its Monte Carlo simulation," *Asia-Pacific International Symposium on Electromagnetic Compatibility (APEMC)*, pp. 779-781, 2016.

[15] Y. Zhao, X. Zhao, L. Yan, C. Liu, K. Huang, Q. Liu, and H. Zhou "Analysis of field-to-transmission line coupling inside a reverberation chamber based on mode expansion method," *IEEE International Symposium on Electromagnetic Compatibility and IEEE Asia-Pacific Symposium on Electromagnetic Compatibility (EMC/APEMC)*, pp. 84-87, 2018.

[16] I. Flintoft, A. Marvin, and L. Dawson, "Statistical response of nonlinear equipment in a reverberation chamber," *IEEE International Symposium on Electromagnetic Compatibility*, pp. 1-6, 2008.

[17] Y. Cui, H. G. Wei, S. Wang, and L. Fan, "Efficient method of optimizing reverberation chamber using FDTD and genetic algorithm method," *Applied Computational Electromagnetics Society Journal*, vol. 28, no. 4, pp. 293-299, Apr. 2013.

[18] J. Clegg, A. C. Marvin, J. F. Dawson, and S. J. Porter, "Optimization of stirrer designs in a reverberation chamber," *IEEE Trans. Electromagn. Compat.*, vol. 47, no. 4, pp. 824-832, Nov. 2005.

[19] L. Bastianelli, V. M. Primiani, and F. Moglie, "Stirrer efficiency as a function of its axis orientation," *IEEE Trans. Electromagn. Compat.*, vol. 57, no. 6, pp. 1732-1735, Dec. 2015.

[20] V. Mariani Primiani and F. Moglie, "Reverberation chamber performance varying the position of the stirrer rotation axis," *IEEE Trans. Electromagn. Compat.*, vol. 56, no. 2, pp. 486-489, Apr. 2014.

[21] G. Bosco, C. Picciani, V. M. Primiani, and F. Moglie, "Numerical and experimental analysis of the performance of a reduced surface stirrer for reverberation chambers," *IEEE International Symposium on Electromagnetic Compatibility*, pp. 156-161, 2012.

[22] H. K. Khattak, P. Bianucci, and A. D. Slepkov, "Linking plasma formation in grapes to microwave resonances of aqueous dimers," *Proceedings of the National Academy of Sciences*, vol. 116, no. 10, pp. 4000-4005, Mar. 2019.

[23] G. Gradoni, T. M. Antonsen, S. M. Anlage, and E. Ott, "A statistical model for the excitation of cavities through apertures," *IEEE Trans. Electromagn. Compat.*, vol. 57, no. 5, pp. 1049-1061, Oct. 2015.